

**Momentum and heat flux events in compressible turbulent channel flows**Cheng Cheng <sup>1</sup>, Wei Shyy,<sup>1</sup> and Lin Fu <sup>1,2,3,4,\*</sup><sup>1</sup>*Department of Mechanical and Aerospace Engineering, The Hong Kong University of Science and Technology, Clear Water Bay, Kowloon, Hong Kong*<sup>2</sup>*Department of Mathematics, The Hong Kong University of Science and Technology, Clear Water Bay, Kowloon, Hong Kong*<sup>3</sup>*HKUST Shenzhen-Hong Kong Collaborative Innovation Research Institute, Futian, Shenzhen, China*<sup>4</sup>*Center for Ocean Research in Hong Kong and Macau (CORE), The Hong Kong University of Science and Technology, Clear Water Bay, Kowloon, Hong Kong*

(Received 25 April 2023; accepted 28 August 2023; published 22 September 2023)

In the present study, the momentum and heat fluxes (MF and HF) in subsonic or supersonic channel flows are studied and compared via resorting to the established analysis tools developed for incompressible flows, such as the conditional sampling and the spectral linear stochastic estimation, by leveraging the newly built database. Particular attention is paid to clarifying the effects of the inner-outer scale interactions on the statistical characteristics of MF and HF in the near-wall and logarithmic regions. To this end, by employing the spectral linear stochastic estimation, the near-wall fluxes are decomposed into large- and small-scale components, and the logarithmic-region fluxes are decomposed into active and inactive parts, respectively. For the near-wall region, the large-scale component is found to be the footprints of large-scale eddies and rather uniform in physical space, whereas the remaining small-scale component is uneven in space and includes the strong transports of momentum and heat in the near-wall region. For the logarithmic region, both the inactive and active components of MF and HF are found to contribute to their mean flux. In the outer region, the ejections of HF are remarkably stronger than those of the MF, and the former is more sparse in the physical space. Reynolds number is shown to have a minor effect on the statistical characteristics of the two fluxes, and the enlargement of the Mach number only appears to lessen the linkages between the inner and outer region fluxes, adjust the proportions of the inactive and active components in the logarithmic region, and rarely alter the overall properties of them. The findings of the present study may contribute to the development of the modeling approach in compressible wall turbulence.

DOI: [10.1103/PhysRevFluids.8.094602](https://doi.org/10.1103/PhysRevFluids.8.094602)**I. INTRODUCTION AND MOTIVATION**

One of the most typical properties of turbulent flows in comparison to laminar flows is the increase of transport processes, particularly momentum and heat. Intrinsically, the wall-normal transportations of the momentum and heat fluxes (denoted as MF and HF hereafter) are responsible for the generation of the wall friction and heat in high-speed flow, respectively. Uncovering their fundamental properties can be revealing to the development of the flow-control strategies and the modeling approaches. Previous studies largely focus on the statistical characteristics of the MF in incompressible flows [1–4], whereas few works are concentrated on the MF and the HF in compressible wall turbulence. The objective of the present study is to fill this gap. We will compare

---

\*Corresponding author: [linfu@ust.hk](mailto:linfu@ust.hk)

the basic characteristics of the MF and the HF in subsonic or supersonic channel flows via resorting to the matured analysis tools developed in previous studies for incompressible flows by leveraging the newly built database [5].

From the 1970s, to shed light on the coherent structures associated with the bursting of the near-wall low-speed streaks [6], several conditional sampling techniques were developed successively to analyze the Reynolds stress (i.e., MF) in incompressible wall turbulence. For example, the quadrant analysis [1,2,7], the variable interval time average [8], the u-level detection [7], and the variable interval space average [9], to name a few. Bogard and Tiederman [10] examined these methods in detail and concluded that the quadrant analysis has the greatest reliability with a high probability of detecting the ejections and a low probability of false detections among these techniques. In this methodology, the signals of the Reynolds stress are classified into four quadrants as per the signs of the streamwise ( $u'$ ) and wall-normal ( $v'$ ) velocity fluctuations: (1)  $Q_{m1}$ , outward interactions with  $u' > 0$  and  $v' > 0$ ; (2)  $Q_{m2}$ , ejections with  $u' < 0$  and  $v' > 0$ ; (3)  $Q_{m3}$ , inward interactions with  $u' < 0$  and  $v' < 0$ ; and (4)  $Q_{m4}$ , sweeps with  $u' > 0$  and  $v' < 0$ . The subscript “m” stands for the momentum flux, and we also use the subscript “h” to represent the heat flux in the present study herein. Among these four quadrants, it turns out that  $Q_{m2}$  and  $Q_{m4}$  contribute more to the mean MF than other two quadrants within the near-wall region [1,2]. By conditional sampling and sorting the signals of MF into four quadrants, Lu and Willmarth [7] further observed that the intense events ( $|u'v'| > 4|u'v'|$ ) only exist in  $Q_{m2}$  and  $Q_{m4}$ , and only 45% of the total samples have a magnitude larger than 0.5  $|u'v'|$ , and they account for nearly 99% of the mean flux  $u'v'$ . All these observations indicate that the MF in the near-wall region is highly intermittent.

The above-mentioned pioneer studies mainly focus on the Reynolds stress in the near-wall region. With the development of computing power and experimental technology, more and more works are dedicated to the bursting and the connected MF in the logarithmic and outer regions. For example, Narasimha *et al.* [3] identified Reynolds-stress structures within the logarithmic layer of the mean flow in the atmospheric boundary layer and evidenced that their length is comparable to the distance to the wall. Flores and Jiménez [11] demonstrated that there exists a hierarchy of bursting in the logarithmic region of the high-Reynolds-number channel flow, in conjunction with quasiperiodic  $Q_{m2}$  and  $Q_{m4}$  events. Lozano-Durán *et al.* [12] also observed that  $Q_{m2}$  and  $Q_{m4}$  events are exhibited as a side-by-side pair in the logarithmic region, and their geometrical characteristics resemble the conjectured attached eddies of Townsend [13]. These studies underline the fact that the MF in the logarithmic region is inextricably linked with the attached eddies.

According to the celebrated attached-eddy model (AEM) proposed by Townsend [13], the logarithmic region of a turbulent boundary layer is occupied by an array of self-similar energy-containing motions (or eddies) with their roots attached to the near-wall region. Townsend [13,14] also pointed out that the motions at a wall-normal position located in the logarithmic region consist of two components. One is the active component, which is responsible for the turbulent transfer at this wall-normal position, and the other is the inactive component, which does not transfer momentum. Deshpande *et al.* [15] showed that the inactive part consists of the self-similar attached eddies as well as the very-large-scale motions (VLSMs), whereas the active part involves the eddies that interact with the local  $v'$ . Seen in this regard, it is sensible to study these two components separately when considering the statistical characteristics of the MF in the logarithmic region. Very recently, Deshpande and Marusic [4] scrutinized these two components of MF in an experimental database of incompressible turbulent boundary layers with friction Reynolds number ranging from  $O(10^3)$  to  $O(10^4)$ . They found that the active component is the dominant contributor to the mean flux, which is in accordance with the AEM, whereas the contribution of the inactive component is nonzero. They ascribed this deviation to the scale interactions and the effects of the VLSMs. Considering the physical properties of the attached eddies and the existing inner-outer interactions, the near-wall MF should also be decomposed into two parts, because it has been shown that the motions populating the logarithmic and outer regions can exert footprints on the near-wall flow [16–18]. Separating the near-wall MF into large-scale footprints and small-scale components, and dissecting them separately, can further shed light on the statistical characteristics of the MF in the

TABLE I. Parameter settings of the compressible DNS database. Here  $M_b$  denotes the bulk Mach number.  $Re_b$ ,  $Re_\tau$ , and  $Re_\tau^*$  denote the bulk Reynolds number, friction Reynolds number, and semilocal friction Reynolds number, respectively.  $\Delta x^+$  and  $\Delta z^+$  denote the streamwise and spanwise grid resolutions in viscous units, respectively.  $\Delta y_{\min}^+$  and  $\Delta y_{\max}^+$  denote the finest and the coarsest resolution in the wall-normal direction, respectively.  $Tu_\tau/h$  indicates the total eddy turnover time used to accumulate statistics.

Case	$M_b$	$Re_b$	$Re_\tau$	$Re_\tau^*$	$\Delta x^+$	$\Delta z^+$	$\Delta y_{\min}^+$	$\Delta y_{\max}^+$	$Tu_\tau/h$
Ma08Re3K	0.8	3000	192	168	8.9	4.5	0.43	4.5	39.5
Ma08Re8K	0.8	7667	436	382	10.8	6.9	0.44	5.4	49.4
Ma08Re17K	0.8	17 000	882	778	10.8	6.5	0.63	6.4	15.3
Ma15Re3K	1.5	3000	220	148	10.8	6.9	0.33	8.2	19.5
Ma15Re9K	1.5	9400	594	395	7.3	3.7	0.5	5.9	30.2
Ma15Re20K	1.5	20 020	1150	780	9.3	4.7	0.49	6.9	9.1
Ma30Re5K	3.0	4880	446	148	8.0	4.0	0.47	5.5	24.1

vicinity of the wall. This is one part of the present study, which is also a complement to the previous studies.

For compressible wall turbulence, according to Ref. [19], the temperature fluctuation can be envisioned as a wall-attached variable, similarly to the streamwise velocity fluctuation. This proposition has been supported by some studies recently [5,20,21]. It suggests that the HF in compressible flow can be dissected just like the MF in incompressible flow. If so, then a question may be raised, that is, How similar and different are the MF and the HF in compressible wall turbulence? This question has not been well clarified yet. In recent years, the database of the compressible turbulent channel flows at various Mach numbers and Reynolds numbers has been built by the authors and other research groups [5,22,23], which can serve as a building block for studying and comparing the statistical characteristics of the MF and the HF in compressible wall turbulence. The analysis tools developed in previous studies for incompressible flows can be employed. Concurrently, the Mach number and Reynolds number effects on MF and HF can also be clarified. This is the motivation of the present work. The findings of the present study may be helpful for the development of the modeling approach in compressible wall turbulence [24,25].

## II. DNS DATABASE

In the present study, we carry out three simulations of supersonic channel flows at a bulk Mach number  $M_b = U_b/C_w = 1.5$  ( $U_b$  is the bulk velocity and  $C_w$  is the speed of sound at wall temperature) and  $Re_b = \rho_b U_b h / \mu_w = 3000, 9400, \text{ and } 20\,020$  ( $\rho_b$  denotes the bulk density,  $h$  the channel half-height, and  $\mu_w$  the dynamic viscosity at the wall). A series of direct numerical simulations (DNS) at a bulk Mach number  $M_b = 0.8$  and  $Re_b = 3000, Re_b = 7667, \text{ and } Re_b = 17\,000$  are also conducted. Additionally, we also perform a DNS at a bulk Mach number  $M_b = 3.0$  and  $Re_b = 4880$ . All these cases are performed in a computational domain of  $4\pi h \times 2\pi h \times 2h$  in the streamwise ( $x$ ), spanwise ( $z$ ), and wall-normal ( $y$ ) directions, respectively. Details of the parameter settings of the formed database are listed in Table I. The maximum number of grid points is in excess of one billion. The validations of the solver are provided in our previous work [5,26], and a brief description of the computational setups can also be found in these papers. One incompressible case  $Re_\tau = 934$  by Del Álamo *et al.* [27] is also employed for comparison. Details of the parameter settings are listed in Table II.

The Reynolds averaged statistics (denoted as  $\bar{\phi}$ ) are used in the present study. The corresponding fluctuating components are represented as  $\phi'$ . Hereafter, we use the superscript  $+$  to represent the normalization with  $\rho_w$ , the friction velocity (denoted as  $u_\tau$ ,  $u_\tau = \sqrt{\tau_w / \rho_w}$ ,  $\tau_w$  is the mean wall-shear stress), the friction temperature (denoted as  $T_\tau$ ,  $T_\tau = Q_w / \rho_w c_p u_\tau$ , where  $Q_w$  and  $c_p$  are the mean heat flux on the wall and the specific heat at constant pressure, respectively), and

TABLE II. Parameter settings of the incompressible DNS database.

Case	$\text{Re}_\tau$	$\text{Re}_\tau^*$	$L_x(h)$	$L_y(h)$	$L_z(h)$	$\Delta x^+$	$\Delta z^+$	$\Delta y_{\min}^+$	$\Delta y_{\max}^+$	$Tu_\tau/h$
Ma00Re18K	934	934	$8\pi$	2	$3\pi$	11.5	5.7	0.03	7.6	12

the viscous length scale (denoted as  $\delta_v$ ,  $\delta_v = \nu_w/u_\tau$ ,  $\nu_w = \mu_w/\rho_w$ ). We also use the superscript  $*$  to represent the normalization with the semilocal wall units, i.e.,  $u_\tau^* = \sqrt{\tau_w/\bar{\rho}}$  and  $\delta_v^* = \overline{v(y)}/u_\tau^*$ . Thus, the relationship between the semilocal friction Reynolds number and the friction Reynolds number is  $\text{Re}_\tau^* = \text{Re}_\tau \sqrt{(\bar{\rho}_c/\bar{\rho}_w)/(\bar{\mu}_c/\bar{\mu}_w)}$ . The subscript  $c$  refers to the quantities evaluated at the channel center. It is noted that the cases of Ma08Re3K, Ma08Re8K, and Ma08Re17K share similar  $\text{Re}_\tau^*$  with the cases of Ma15Re3K, Ma15Re9K, and Ma15Re20K, respectively. The case Ma30Re5K bears similar  $\text{Re}_\tau^*$  with the cases of Ma15Re3K and Ma08Re3K. In the present study, we mainly adopt the cases with  $M_b = 1.5$  to investigate the momentum and heat flux events in compressible wall turbulence, whereas the other cases (include the incompressible case, and the cases with  $M_b = 0.8$  and  $M_b = 3.0$ ) primarily aid in elucidating the Mach number effects on the statistics. Besides, previous studies [28–31] pointed out that the semilocal scalings,  $\text{Re}_\tau^*$  and  $y^*$ , can reasonably clarify the Reynolds number effects on the statistics involving the thermodynamic and the velocity variables in compressible channel flows. Hence, we adopt them more frequently than  $\text{Re}_\tau$  and  $y^+$  in the present study. Additionally, to account for the density variation in compressible flows, the density-weighted streamwise velocity fluctuation ( $\sqrt{\rho}u'$ , denoted as  $u'_d$ ), wall-normal velocity fluctuation ( $\sqrt{\rho}v'$ , denoted as  $v'_d$ ), and temperature fluctuation ( $\sqrt{\rho}T'$ , denoted as  $T'_d$ ) are employed to calculate the MF and the HF. We also have checked that there is a negligible difference between the Reynolds and Favre averaged velocity fluctuations in the cases under scrutinizing.

### III. METHODOLOGIES

#### A. Conditional sampling technique

The first analysis tool is the conditional sampling technique, which is rather mature in investigating the statistical characteristics of the MF in incompressible wall turbulence [1–4]. The present study can be considered as its extension in compressible-flow research. We take the MF in compressible flow as an example to show its procedures, and the processing of HF can be constructed similarly.

(1) First, a test function  $\delta_i(x, y, z)$  is introduced to distinguish which quadrant ( $Q_{m1}$ – $Q_{m4}$ ) an instantaneous momentum flux  $u'_d v'_d(x, y, z)$  belongs to.  $\delta_i(t)$  can be expressed as [4]

$$\delta_i(x, y, z) \equiv \begin{cases} 1 & (u'_d(x, y, z), v'_d(x, y, z)) \text{ is in quadrant } Q_{mi} \text{ of the } u'_d\text{-}v'_d \text{ plane} \\ 0 & \text{otherwise} \end{cases}, \quad (1)$$

where  $i = 1, 2, 3$ , and 4. After this operation, the conditional momentum flux is

$$[u'_d v'_d(x, y, z)] = \delta_i(x, y, z) u'_d v'_d(x, y, z). \quad (2)$$

(2) Second, following previous works [2,3], a momentum flux event is identified when

$$|u'_d v'_d(x, y, z)| > k_f (u'_d v'_d)_{rms}(y), \quad (3)$$

where  $k_f$  is a positive threshold, and  $(u'_d v'_d)_{rms}$  denotes the root-mean-square value of  $u'_d v'_d$ . Thus, the fractional contribution (FC) to mean flux ( $\overline{u'_d v'_d}$ ) from the events identified by Eq. (3) can be calculated by

$$\text{FC}_m(k_f) = \frac{1}{N_t \overline{u'_d v'_d}} \sum_{j=1}^{N(k_f)} (u'_d v'_d)_j, \quad (4)$$

where the subscript “m” represents the momentum flux,  $N_t$  denotes the total number of the samples under counting, and  $N(k_f)$  denotes the total number of the events detected by Eq. (3) at a given  $k_f$  with  $(u'_d v'_d)_j$  being the magnitude of the  $j$ th event. Moreover, the spatial duration (SD) of identified events can also be defined as

$$SD_m(k_f) = \frac{N(k_f)}{N_t}. \quad (5)$$

It is not difficult to find that  $FC_m(0) = 1$  and  $SD_m(0) = 1$ , as no event is ruled out by Eq. (3) when  $k_f = 0$ . It is noted that experimental studies regularly measure the time duration [3,4]. To leverage the merits of the numerical simulation, we inspect the spatial duration instead.

(3) Finally, combining steps (1) and (2), the fractional contribution from the events residing in quadrant  $Q_{mi}$  can also be calculated as

$$FC_{mi}(k_f) = \frac{1}{N_t \overline{u'_d v'_d}} \sum_{j=1}^{N_i(k_f)} [u'_d v'_d]_j, \quad (6)$$

where  $N_i(k_f)$  denotes the total number of the events which belong to quadrant  $Q_{mi}$  and are detected by Eq. (3) at a given  $k_f$ .  $[u'_d v'_d]_j$  is the  $j$ th event which meets these two conditions.

The conditional sampling technique described above can shed light on some statistical characteristics of MF and HF events generally, such as their frequencies of occurrence, amplitude magnitudes, and fractional contributions.

### B. Scale measuring method

It can be envisioned that, in a wall-parallel ( $x$ - $z$ ) plane, the instantaneous events belonging to a quadrant may be continuous in the streamwise direction. Thus, it is sensible to measure their spatial length. We also take the MF in compressible flow as an example to elaborate the method employed here, and the processing of HF can also be constructed similarly.

(1) The events identified by Eq. (3) can be further categorized as the quadrant they belong to, as per the signs of  $u'_d$  and  $v'_d$ . Here the threshold  $k_f$  is fixed at 0.25 to keep in line with previous studies in incompressible wall turbulence [4]. We will also demonstrate its justification in the present database in Sec. IV.

(2) The events marked in step (1), which are contiguous in the streamwise direction, are connected into individual structures.

(3) Each structure identified in step (2) has a streamwise length scale  $l_x$ , which can be treated as the characteristic length scale of this structure.

### C. Scale decomposition method

According to the AEM, the active component at  $y_p$  in the logarithmic region is representative of the attached eddies with their wall-normal heights equal to  $y_p$  (interact with wall-normal velocity  $v'$  at  $y_p$ ). On the other hand, the inactive part stems from those tall and large attached eddies with their heights within the interval  $[y_p, h]$  [15] (cannot interact with  $v'$  at  $y_p$ ), which impose influences on the streamwise and spanwise velocity components. Moreover, according to Ref. [19], the temperature fluctuation in compressible wall turbulence can be envisioned as a wall-attached variable, similarly to the streamwise velocity fluctuation. Thus, the MF and the HF in the logarithmic region can be decomposed as [4]

$$\overline{u'_d v'_d} = \overline{u'_{d,a} v'_d} + \overline{u'_{d,ia} v'_d}, \quad (7)$$

$$\overline{T'_d v'_d} = \overline{T'_{d,a} v'_d} + \overline{T'_{d,ia} v'_d}, \quad (8)$$

where the subscripts “a” and “ia” represent the active and inactive components, respectively. Both the second terms on the right-hand sides of Eq. (7) and Eq. (8) should be trivial within the AEM

framework for incompressible wall turbulence. Whether it is true in compressible wall turbulence remains to be checked.

In the present study, we resort to the spectral linear stochastic estimation (SLSE) to decompose the temperature and velocity fields in the logarithmic region into the active and inactive components. The DNS instantaneous fields at a given wall-normal height can be decomposed into Fourier coefficients along the streamwise and spanwise directions by leveraging the homogeneity along these two directions. The inactive component of a physical quantity  $\psi$  ( $\psi$  can be  $u'_d$  and  $T'_d$  in the present study) in the logarithmic region  $y_p$  can also be estimated by

$$\psi_{ia}(y_i, y_p) = F_{x,z}^{-1}\{H_{ia}(\lambda_x, \lambda_z; y_i, y_p)F_{x,z}[\psi(y_i)]\}, \quad (9)$$

where  $F_{x,z}$  and  $F_{x,z}^{-1}$  denote the two-dimensional fast Fourier transform (2D FFT) and the inverse 2D FFT in the streamwise and spanwise directions, respectively.  $y_i$  is a wall-normal location in the near-wall region and set as  $y_i^* = 10$  (i.e.,  $y_i^+ = 14$ ) in the present study. Prior studies have shown that the wall coherence of  $\psi$  in the logarithmic region remains largely unchanged when  $0 \leq y_i^+ \leq 15$  [32].  $H_{ia}$  is a transfer kernel, which evaluates the correlation between  $\hat{\psi}(y_i)$  and  $\hat{\psi}(y_p)$  at streamwise length scale  $\lambda_x$  and spanwise length scale  $\lambda_z$ , and can be calculated as

$$H_{ia}(\lambda_x, \lambda_z; y_i, y_p) = \frac{\langle \hat{\psi}(\lambda_x, \lambda_z; y_p) \check{\psi}(\lambda_x, \lambda_z; y_i) \rangle}{\langle \hat{\psi}(\lambda_x, \lambda_z; y_i) \check{\psi}(\lambda_x, \lambda_z; y_i) \rangle}, \quad (10)$$

where  $\langle \cdot \rangle$  represents the ensemble averaging,  $\hat{\psi}$  is the Fourier coefficient of  $\psi$ , and  $\check{\psi}$  is the complex conjugate of  $\hat{\psi}$ . Consequently,  $\psi_a(y_p) = \psi(y_p) - \psi_{ia}(y_i, y_p)$  is the active component.

On the other hand, due to the characteristics of the attached eddies, it is obvious that the inactive component at  $y_p$  would exert footprints on the near-wall flow at  $y_i$  [17]. These large-scale footprints  $\psi_L$  can be estimated by

$$\psi_L(y_p, y_i) = F_{x,z}^{-1}\{H_L(\lambda_x, \lambda_z; y_p, y_i)F_{x,z}[\psi(y_p)]\}, \quad (11)$$

with

$$H_L(\lambda_x, \lambda_z; y_p, y_i) = \frac{\langle \hat{\psi}(\lambda_x, \lambda_z; y_i) \check{\psi}(\lambda_x, \lambda_z; y_p) \rangle}{\langle \hat{\psi}(\lambda_x, \lambda_z; y_p) \check{\psi}(\lambda_x, \lambda_z; y_p) \rangle}. \quad (12)$$

In this respect,  $\psi_s(y_i) = \psi(y_i) - \psi_L(y_p, y_i)$  is the remained small-scale component. Equation (11) and Eq. (12) constitute a decomposition scheme for the near-wall flow. Thus, the near-wall MF and HF can be decomposed according to

$$\overline{u'_d v'_d} = \overline{u'_{d,s} v'_{d,s}} + \overline{u'_{d,L} v'_{d,L}}, \quad (13)$$

$$\overline{T'_d v'_d} = \overline{T'_{d,s} v'_{d,s}} + \overline{T'_{d,L} v'_{d,L}}, \quad (14)$$

where  $\overline{u'_{d,s} v'_{d,s}}$  and  $\overline{T'_{d,s} v'_{d,s}}$  denote the MF and the HF generated by the near-wall small-scale motions, and  $\overline{u'_{d,L} v'_{d,L}}$  and  $\overline{T'_{d,L} v'_{d,L}}$  are the counterparts contributed by the large-scale footprints. These terms can be investigated separately. Similar methodologies are employed by the authors to investigate the physical characteristics of the attached eddies in incompressible wall-bounded turbulence [18,33].

## IV. RESULTS

### A. Near-wall region

Figures 1(a) and 1(b) show the variations of the fractional contributions FC and the spatial duration SD as functions of the threshold  $k_f$  for the MF and the HF at  $y^* = 10$ , respectively. The variation tendencies of FCs for these two fluxes are not altered significantly as the increment of the Reynolds number. Minor Reynolds number dependence can also be observed for SDs. That is, these

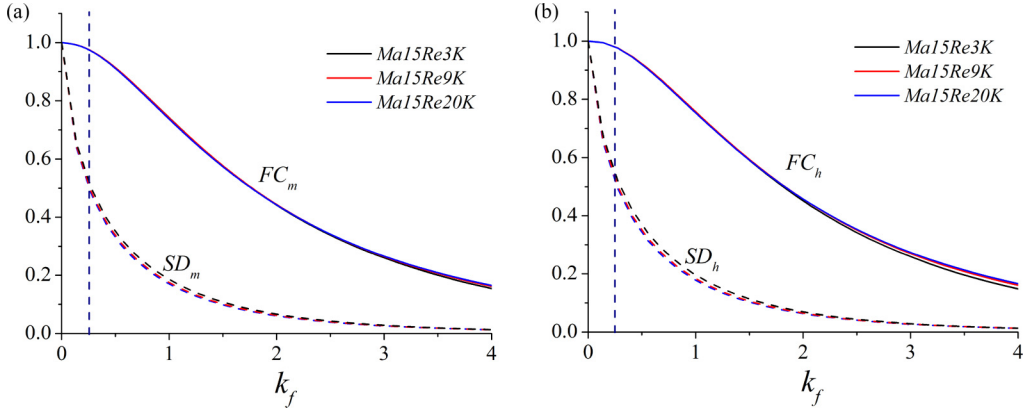


FIG. 1. Variations of the fractional contribution (FC) to the mean flux and the spatial duration (SD) of (a) MF, and (b) HF as functions of  $k_f$  at  $y^* = 10$ . The data are taken from the cases with  $M_b = 1.5$ . The vertical dashed lines in the figures highlight  $k_f = 0.25$ .

two basic properties of the momentum and heat transfers in the near-wall region are insensitive to the Reynolds number, just like the observation in the near-wall region of the incompressible wall turbulence [1]. Though as the increase of the Reynolds number, more and more  $u'_d$  and  $T'_d$  motions populating the logarithmic region would penetrate into the near-wall region, the locality of the  $v'_d$  would diminish the Reynolds-number effects on the statistical characteristics of the momentum and heat fluxes [34,35]. On the other hand, the magnitudes of the two fluxes are not large in most of the physical space, and the extreme events are scarce. Taking MF as an example, when  $k_f = 0.25$ , over 95% of the mean flux can be recovered by nearly 50% samples for all three cases. It also signifies that  $k_f = 0.25$  is an optimal, Re-independent threshold for the MF and the HF in the near-wall region.

MF and HF can be further divided into four quadrants, and their statistical characteristics can be studied separately. Figures 2(a) and 2(b) display the  $FC_{mi}$  and the  $FC_{hi}$  for  $i = 1 - 4$  at  $y^* = 10$ , respectively. Their definitions are given by Eq. (6). It is evident that the sweeps ( $Q_{m4}$  and  $Q_{h4}$ ) contribute more to the mean flux than ejections ( $Q_{m2}$  and  $Q_{h2}$ ), regardless of the Reynolds number. This phenomenon can be ascribed to the blockage of the wall surface in the vicinity of the wall.

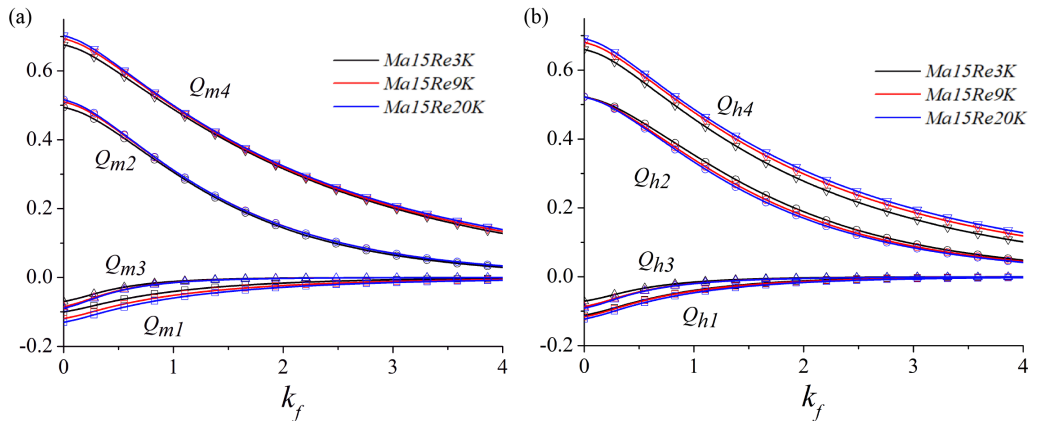


FIG. 2. Variations of the fractional contribution to the mean flux from the four quadrants of (a) MF and (b) HF as functions of  $k_f$  at  $y^* = 10$ . The data are taken from the cases with  $M_b = 1.5$ .

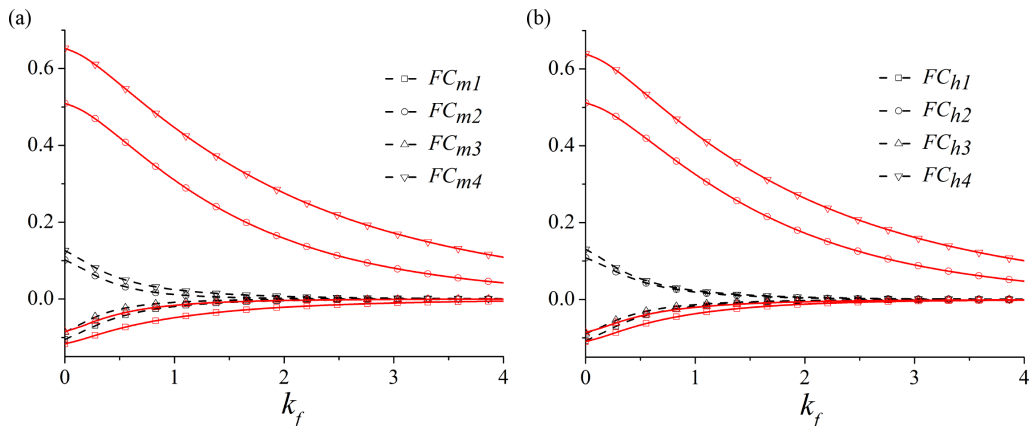


FIG. 3. Variations of the fractional contribution to the mean flux from the four quadrants of the large- (black dashed lines) and small-scale (red solid lines) components of (a) MF and (b) HF as functions of  $k_f$  at  $y^* = 10$ . The data are taken from the case Ma15Re20K.

Moreover, it can also be delineated by the celebrated hairpin vortex model. The dominated sweeps are generated by the legs of the hairpins in the vicinity of the wall [36]. The variation of the Reynolds number chiefly affects the fractional contribution from sweeps for both MF and HF. To be specific, for MF, the increase of  $Re_b$  leads to a larger contribution from  $Q_{m4}$  when  $k_f \leq 1$ , whereas for HF, a similar Reynolds number dependence can be observed for larger  $k_f$ . It indicates that the Reynolds number dependence of the intense sweeps is more conspicuous for HF than those of MF in the near-wall region. In incompressible wall turbulence, it has been demonstrated that the Reynolds number effects of the near-wall turbulence result from the influences exerted by the eddies populating the logarithmic and the outer regions [18,37,38]. Thus, the decomposition schemes Eq. (11) and Eq. (12) can be employed to further shed light on this effect. The MF and the HF at  $y^* = 10$  can be decomposed into large- and small-scale components as per Eq. (13) and Eq. (14) by setting  $y_i^* = 10$  and  $y_p^* = 100$  (the lower boundary of the logarithmic region [39]) in Eq. (11) and Eq. (12). Then the small-scale components  $u'_{d,s}v'_d$  and  $T'_{d,s}v'_d$  and the large-scale footprints  $u'_{d,L}v'_d$  and  $T'_{d,L}v'_d$  are treated as the input signals of the conditional sampling method described in Sec. III A. The fractional contributions from these decomposed signals residing in four quadrants are shown in Figs. 3(a) and 3(b) for MF and HF at  $y^* = 10$  for the case Ma15Re20K, respectively. The reason we only use the case Ma15Re20K is due to its relatively higher Reynolds number than other cases. It is noteworthy that the variation tendencies of the small-scale fluxes,  $u'_{d,s}v'_d$  and  $T'_{d,s}v'_d$ , resemble those of the original signals displayed in Figs. 2(a) and 2(b) intuitively. Moreover, the nontrivial contribution from each quadrant of the footprints  $u'_{d,L}v'_d$  and  $T'_{d,L}v'_d$  is consistent with the AEM, which hypothesizes that the attached eddies and the energy-containing motions populating the logarithmic and outer regions would permeate into the near-wall region (i.e., the footprints) and interact with the local  $v'_d$  [13]. On the other hand, the net contributions from the footprints  $u'_{d,L}v'_d$  and  $T'_{d,L}v'_d$  are trivial. For example, when  $k_f = 0$ , the contributions from  $u'_{d,L}v'_d$  in four quadrants nearly cancel out each other. The increase of  $k_f$  does not alter this situation, i.e., the absolute value of the contributions from four quadrants are approximately equal. These observations highlight the fact that the footprints originated from the motions populating the logarithmic and outer regions impart limited influences on the magnitudes of the near-wall HF and MF. Another noteworthy observation is the amplitude of each component in each quadrant. When  $k_f > 1$ , the contributions from  $u'_{d,L}v'_d$  and  $T'_{d,L}v'_d$  in four quadrants are vanishing, and only those from sweeps and ejections associated with  $u'_{d,s}v'_d$  and  $T'_{d,s}v'_d$  are non-negligible. It underscores the fact that the intense momentum and heat flux events in the near-wall region are generated by the local small-scale turbulence rather than the

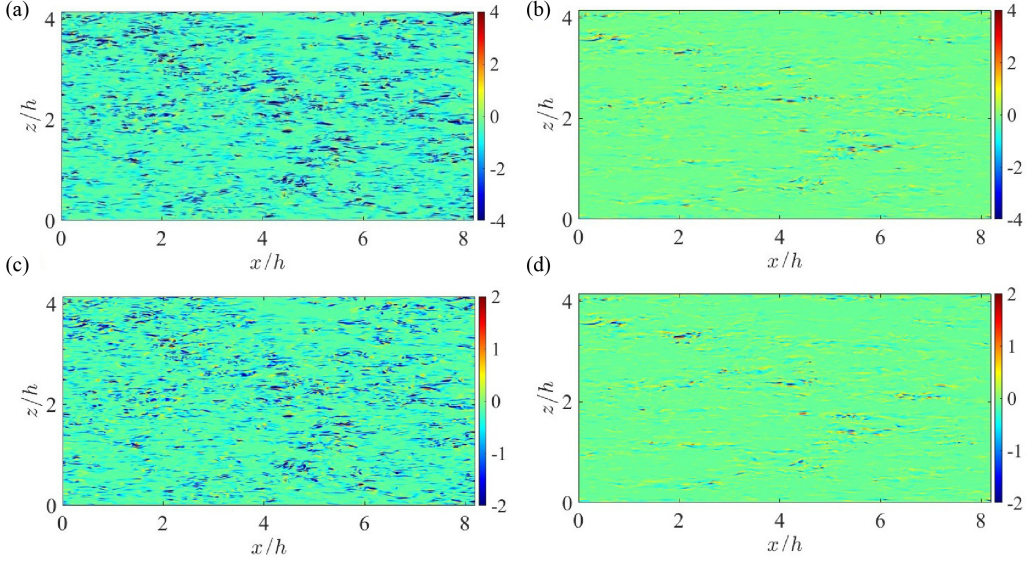


FIG. 4. [(a) and (b)] The instantaneous  $u'_{d,s} v'^+_d$  (a) and  $u'_{d,L} v'^+_d$  (b) at  $y^* = 10$ ; [(c) and (d)] the instantaneous  $T'_{d,s} v'^+_d$  (c) and  $T'_{d,L} v'^+_d$  (d) at  $y^* = 10$ . The data are taken from the case Ma15Re20K.

motions residing above the buffer layer. That is, to control the extreme events in the near-wall region, attention should be paid to the small-scale flow. Figures 4(a) and 4(b) here show the instantaneous  $u'_{d,s} v'^+_d$  and  $u'_{d,L} v'^+_d$  at  $y^* = 10$  in the case Ma15Re20K, respectively, and Fig. 4(c) and Fig. 4(d) display the counterparts of HF, respectively. It is not difficult to observe that the intense momentum and heat flux structures in the near-wall region are mainly contributed by the small-scale signals rather than the footprints of the motions residing above the buffer layer. These visible results are consistent with our analyses.

For the rest of this subsection, we measure the characteristic scale of each signal decomposed above according to the methodology introduced in Sec. III B, and the occurrence frequency of each  $l_x^*$  is exhibited in Fig. 5. Here  $k_f$  is set as 0.25, which is an optimal and Re-invariant threshold as

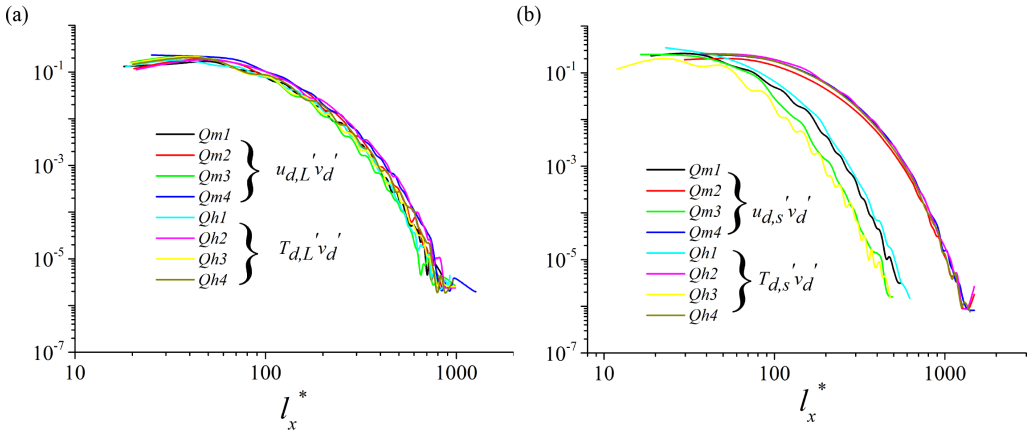


FIG. 5. Occurrence frequency of each  $l_x^*$  for large- (a) and small-scale (b) components of MF and HF from the four quadrants at  $y^* = 10$ . The data are taken from the case Ma15Re20K.

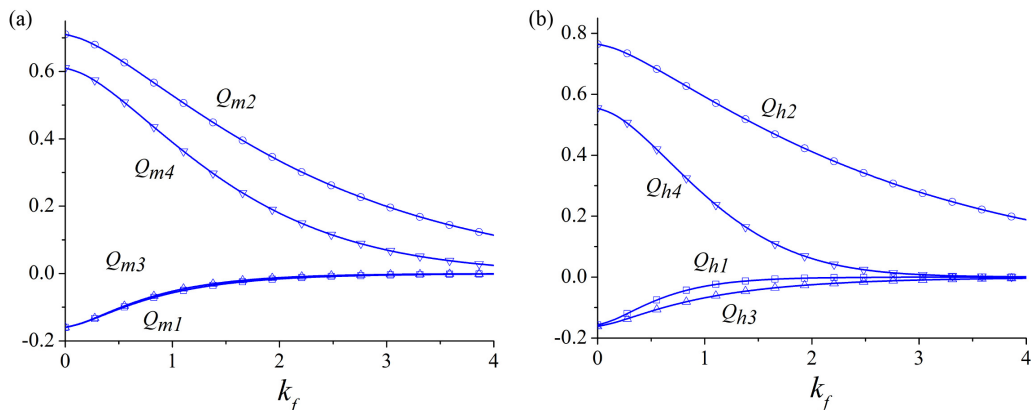


FIG. 6. Variations of the fractional contribution to the mean flux from the four quadrants of (a) MF and (b) HF as functions of  $k_f$  at  $y^* = 3.9\sqrt{\text{Re}_\tau^*}$ . The data are taken from the case Ma15Re20K.

reported by Fig. 1. As can be seen, the  $l_x^*$  of  $u'_{d,L}v'_d$  and  $T'_{d,L}v'_d$  in four quadrants share similar occurrence frequencies, whereas for  $u'_{d,s}v'_d$  and  $T'_{d,s}v'_d$ , those are distinct. Sweeps and ejections associated with  $u'_{d,s}v'_d$  and  $T'_{d,s}v'_d$  tend to have higher frequencies at a given  $l_x^*$  than the events in the other two quadrants. It shows once again that the fluxes generated by the large-scale footprints are rather uniform in physical space, whereas those formed by the local near-wall turbulence are asymmetric for four quadrants. This circumstance is reminiscent of the wall-shear fluctuations generated by the near-wall flow and the attached eddies in incompressible wall-bounded turbulence [18].

Here is a summary: The MF and the HF in the near-wall region of the compressible channel flows are of many similarities. The fractional contribution and spatial duration of them are insensitive to the Reynolds number, at least for the cases considered in this work. The sweeps ( $Q_{m4}$  and  $Q_{h4}$ ) contribute most to their mean flux, regardless of the Reynolds number. Decomposing these two fluxes into large- and small-scale components suggests that the former is the footprints of large-scale eddies and is rather uniform in physical space, whereas the latter is uneven in space and includes the strong transports of momentum and heat in the near-wall region. Last, we conjecture that the Reynolds-number effects cannot influence the fractional contribution and spatial duration of MF and HF remarkably. This is attributed to the fact that the Reynolds-number effects mainly exert influences on  $u'_d$  and  $T'_d$ , whereas the locality of  $v'_d$  would diminish the Reynolds-number effects on the statistical characteristics of the MF and the HF. This hypothesis remains to be examined by new DNS data at higher Reynolds numbers.

## B. Logarithmic region

For the logarithmic region, we only show the results of the case Ma15Re20K due to its relatively higher Reynolds number than other cases. It is observed that the variation tendencies of the fractional contribution and the spatial duration in the logarithmic region agree tolerably well with those in the near-wall region (see Fig. 1). These profiles are not shown here for brevity. It indicates some similarities between these two regions as a whole and verifies the justification of the threshold  $k_f = 0.25$  in the logarithmic region.

However, differences appear when MF and HF are further divided into four quadrants and analyzed separately. Figures 6(a) and 6(b) show the  $FC_{mi}$  and the  $FC_{hi}$  for  $i = 1-4$  at  $y^* = 3.9\sqrt{\text{Re}_\tau^*}$ , namely the center of the logarithmic layer [40] ( $y \approx 0.14h$  for Ma15Re20K), respectively. First, the ejections ( $Q_{m2}$  and  $Q_{h2}$ ) can be observed to be dominant contributors to the mean flux, which is different from the situation in the near-wall region (see Fig. 2). This observation is also in line with

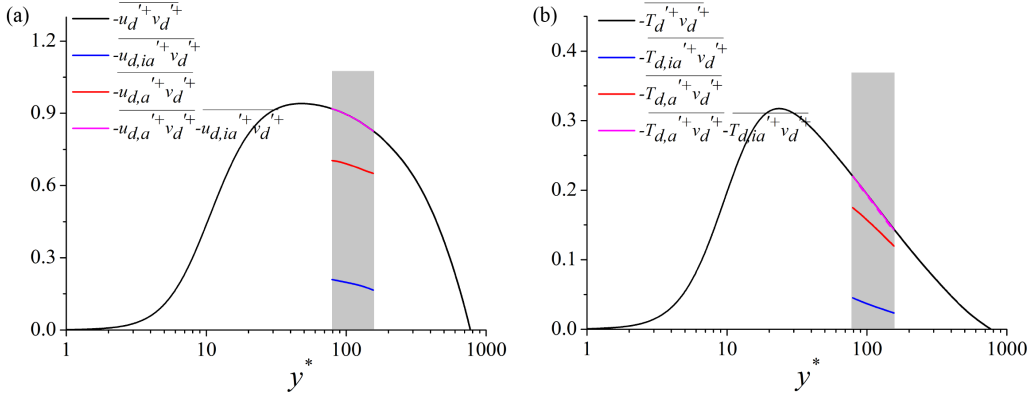


FIG. 7. Variations of the viscous scaled MF (a) and HF (b) as functions of  $y^*$ . MF and HF are decomposed into active and inactive components in the logarithmic region indicated by the shaded regions in the figures. The data are taken from the case Ma15Re20K.

the hairpin vortex model. In the logarithmic region, the hairpins are inclined at an angle to the wall and would eject fluid upward between the lags [36,41]. Second, it is apparent that the ejections of HF are stronger than those of MF. For example, at  $k_f = 0$ , the ejections of MF and HF contribute to nearly 70% and 80% to their mean flux, respectively. Third, the intensities of  $Q_{m1}$  and  $Q_{m3}$  are approximately equal for all  $k_f$  considered, whereas for  $Q_{h1}$  and  $Q_{h3}$  are not.

To further dissect the statistical characteristics of the MF and the HF in the logarithmic region, MF and HF are decomposed into active and inactive parts according to Eq. (7) and Eq. (8), by resorting to the scheme Eq. (9) and Eq. (10) with  $y_i^* = 10$ . The mean flux of each component is exhibited in Fig. 7, and the mean fluxes of full data are also included for comparison. It can be seen that the active component is the chief carrier of the MF and HF, which is consistent with the predictions of the AEM [13,14]. However, the inactive parts, i.e.,  $\overline{u_{d,ia}'^+ v_d'^+}$  and  $\overline{T_{d,ia}'^+ v_d'^+}$ , still have non-negligible contributions to the corresponding mean fluxes. Strictly speaking, this scenario is not consistent with the AEM. Because for a pure attached-eddy occupied flow, the inactive part should play a negligible role in the momentum or heat transfer at the corresponding location in the logarithmic region. For the DNS data analyzed in the present study (Ma15Re20K),  $\overline{u_{d,ia}'^+ v_d'^+}$  nearly contributes to 20% of  $\overline{u_d'^+ v_d'^+}$ , whereas the active component contributes to 80% of  $\overline{u_d'^+ v_d'^+}$ . This scenario has also been reported in incompressible wall turbulence [4]. For the HF, a similar observation can be made.  $\overline{T_{d,ia}'^+ v_d'^+}$  nearly contributes to 18% of  $\overline{T_d'^+ v_d'^+}$  in the logarithmic region. All these indicate that the logarithmic region of wall-bounded turbulence is not fully occupied by the attached eddies. Other eddies, such as the ones that are responsible for the energy dissipation, as well as VLSMs, also influence the magnitudes of  $\overline{u_{d,ia}'^+ v_d'^+}$  and  $\overline{T_{d,ia}'^+ v_d'^+}$  [4]. Figure 8(a) and Fig. 8(b) show the instantaneous  $u_{d,a}'^+ v_d'^+$  and  $u_{d,ia}'^+ v_d'^+$  at  $y^* = 3.9\sqrt{\text{Re}_\tau^*}$  in the case Ma15Re20K, respectively, and Fig. 8(c) and Fig. 8(d) display the counterparts of HF, respectively. As seen, the contributions from the sweep and ejection structures in  $u_{d,a}'^+ v_d'^+$  and  $T_{d,a}'^+ v_d'^+$  are prominent, whereas the corresponding structures in inactive components are rather moderate. These observations are in line with the quantitative analyses above.

The fractional contributions from the active and inactive components residing in different quadrants are shown in Figs. 9(a) and 9(b) for MF and HF at  $y^* = 3.9\sqrt{\text{Re}_\tau^*}$  for the case Ma15Re20K, respectively. The active component resembles the full channel data shown in Fig. 6. This is under expectation because this component is dominant in the momentum transfer according to the AEM. It is particularly noteworthy that the inactive components in four quadrants are not that symmetric. To be specific, the contributions from the second and fourth quadrants (sweeps and ejections) cannot

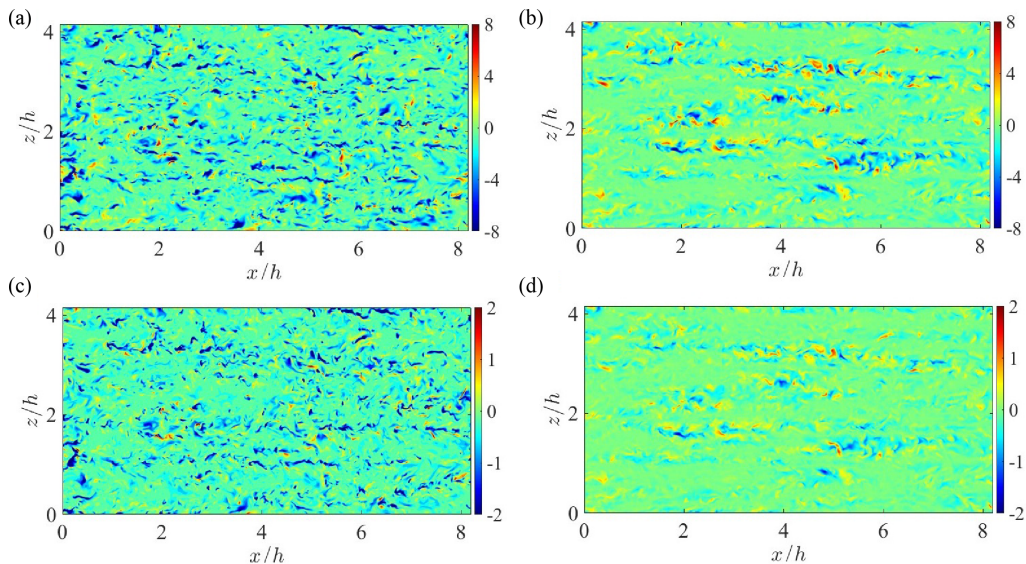


FIG. 8. [(a) and (b)] The instantaneous  $u_{d,a}^+ v_d^+$  (a) and  $u_{d,ia}^+ v_d^+$  (b) at  $y^* = 3.9\sqrt{\text{Re}_\tau^*}$ ; [(c) and (d)] the instantaneous  $T_{d,a}^+ v_d^+$  (c) and  $T_{d,ia}^+ v_d^+$  (d) at  $y^* = 3.9\sqrt{\text{Re}_\tau^*}$ . The data are taken from the case Ma15Re20K.

be canceled by those from the first and third quadrants when  $k_f < 2$ . On the other hand, it is noted that the footprints of these inactive motions in the near-wall region are rather symmetric and uniform for the four quadrants (see black lines in Fig. 3). This is, the distributions of HF and MF in four quadrants resulting from the inactive motions alter significantly when they permeate into the near-wall region. The mechanisms behind this variation deserve further investigation.

Figures 10(a) and 10(b) show the occurrence frequency of each  $l_x/h$  for each decomposed signal in different quadrant. Due to the asymmetric behaviors of the inactive and active parts, the occurrence frequency of each  $l_x/h$  of them in each quadrant are not identical. Sweeps ( $Q_{m4}$  and  $Q_{h4}$ )

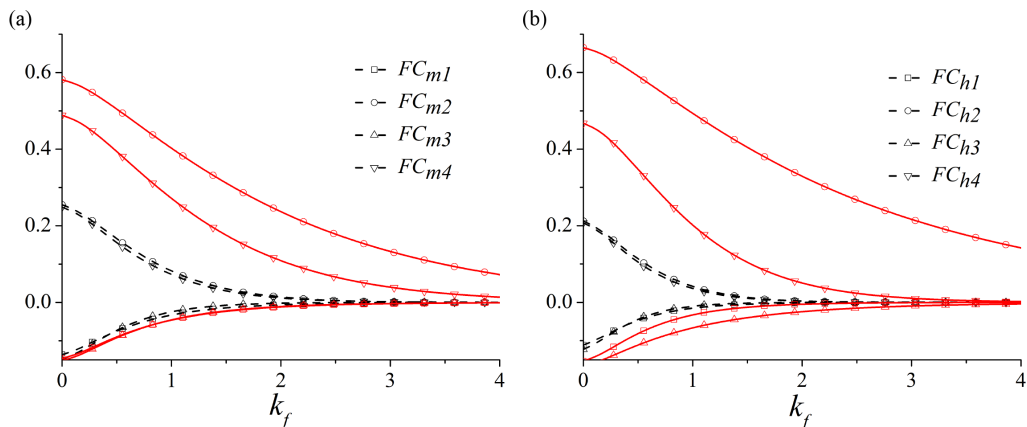


FIG. 9. Variations of the fractional contribution to the mean flux from the four quadrants of the active (red solid lines) and inactive components (black dashed lines) of (a) MF and (b) HF as functions of  $k_f$  at  $y^* = 3.9\sqrt{\text{Re}_\tau^*}$ . The data are taken from the case Ma15Re20K.

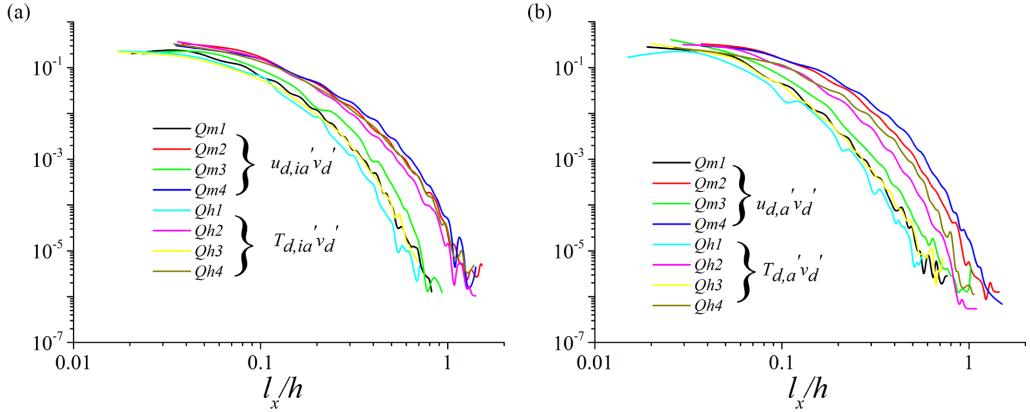


FIG. 10. Occurrence frequency of each  $l_x/h$  for inactive (a) and active (b) components of MF and HF from the four quadrants at  $y^* = 3.9\sqrt{\text{Re}_\tau^*}$ . The data are taken from the case Ma15Re20K.

and ejections ( $Q_{m2}$  and  $Q_{h2}$ ) have higher frequencies at a given  $l_x/h$  than the signals at other two quadrants for both inactive and active components.

In summary, the ejections of HF are stronger than that of MF roughly. Both the inactive and active components of MF and HF have nontrivial contributions to their mean flux. Only the latter is deemed to be responsible for the momentum transfer by the celebrated AEM. Moreover, we also show that these two components are not symmetric among the four quadrants. Considering the footprints of the inactive part in the near-wall region are relatively uniform in four quadrants, this transition awaits further investigations.

### C. Outer region

At last, we are dedicated to the MF and the HF in the outer region at  $y/h = 0.5$ . Figures 11(a) and 11(b) show the  $\text{FC}_{mi}$  and the  $\text{FC}_{hi}$  for  $i = 1-4$  for all cases, respectively. The ejections ( $Q_{m2}$  and  $Q_{h2}$ ) are still the dominant contributors to the mean flux, just like the scenario in the logarithmic region. However, the differences between MF and HF are more conspicuous in this wall-normal position than those in the inner and logarithmic regions. A noteworthy difference is that the ejections

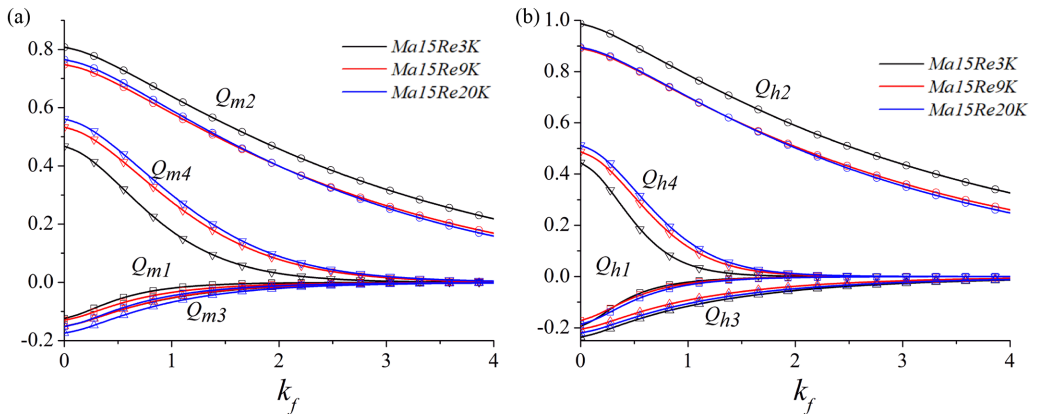


FIG. 11. Variations of the fractional contributions to the mean flux from the four quadrants of (a) MF and (b) HF as functions of  $k_f$  at  $y/h = 0.5$ . The data are taken from the cases with  $M_b = 1.5$ .

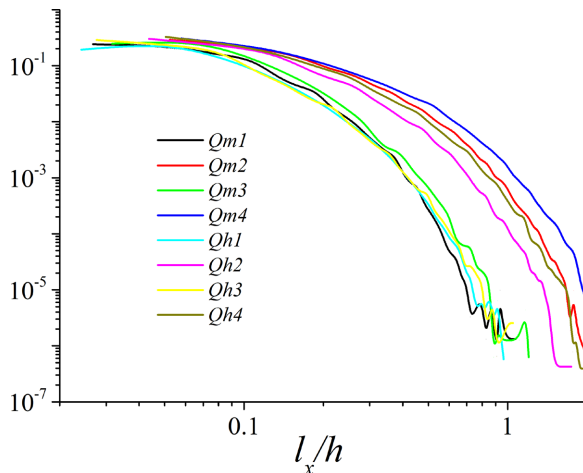


FIG. 12. Occurrence frequency of each  $l_x/h$  for MF and HF from the four quadrants at  $y/h = 0.5$ . The data are taken from the case Ma15Re20K.

of HF ( $Q_{h2}$ ) are remarkably stronger than those of the MF ( $Q_{m2}$ ). Moreover, the intense sweeps ( $k_f > 1$ ) are less for HF. By the way, the profiles of the case Ma15Re3K deviate from those of the two other cases apparently (especially for sweeps and ejections), and it may result from the low-Reynolds-number effects of this case. Figure 12 shows the occurrence frequency of each  $l_x/h$  for the MF and the HF in each quadrant for the case Ma15Re20K. Other cases display similar results and not shown here for brevity. For MF and HF, the occurrence frequency of each  $l_x/h$  for sweeps and ejections is larger. Further observation shows that the occurrence frequency at a given  $l_x/h$  for sweeps and ejections of MF is longer than those of HF. In other words, the HF events in the outer region are more sparse than the MF events.

## V. DISCUSSION ON THE MACH NUMBER EFFECTS

In this section, we concentrate on the Mach number effects on the HF and the MF events. The cases Ma08Re3K, Ma15Re3K, and Ma30Re5K are adopted to elucidate the Mach number effects on the full near-wall fluxes (no decomposition). Our study above demonstrates that the Reynolds number effects are minor in the vicinity of the wall. Thus, these low-Reynolds-number cases are sufficient for pinpointing the Mach number effects. The cases Ma00Re18K, Ma08Re17K, and Ma15Re20K are employed to show the Mach number effects on the logarithmic-region fluxes and their near-wall footprints due to their relatively higher Reynolds numbers. The MF in the incompressible case Ma00Re18K can be used for comparison. We acknowledge that the DNS data with a higher Mach number (for example,  $M_b = 3.0$ ) is needed for conducting a more comprehensive study on this problem. However, the DNS of supersonic channel flows at both high Mach number and Reynolds number demands huge computational costs. A more extensive investigation of the Mach number effects on these aspects will be carried out when the database is available. Finally, the cases with  $Re_\tau^* > 180$  aid in examining the Mach number effects on the fluxes in the outer region to avoid the low-Reynolds-number effects shown in Fig. 11.

We first examine the low-Reynolds-number cases at  $y^* = 10$ . We find that there is no remarkable difference between the variation tendencies of the fractional contributions and spatial duration with respect to  $k_f$  (just like Fig. 1). Moreover, the quadrant analyses also exhibit minor differences among these cases (just like Fig. 2). We can safely conclude that the Mach number has little effect on general statistics of the MF and the HF events within the near-wall region. These results are not shown here for brevity.

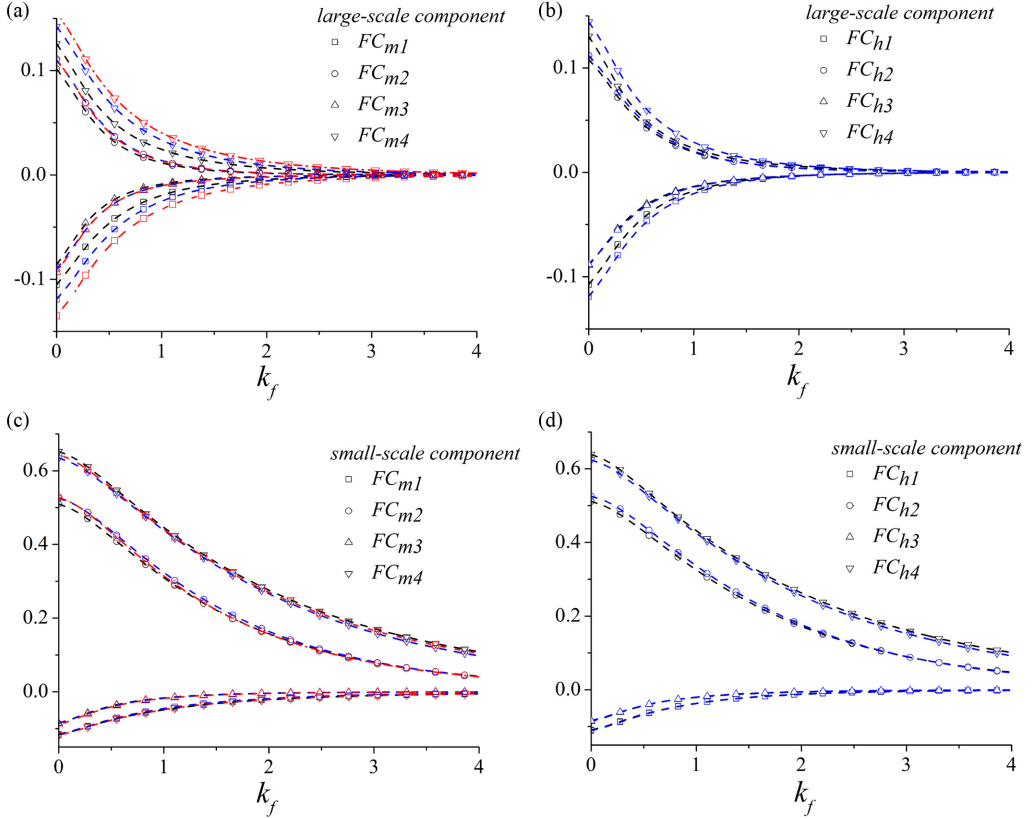


FIG. 13. [(a) and (b)] Variations of the fractional contribution to the mean flux from the four quadrants of the large-scale component of (a) MF and (b) HF as functions of  $k_f$  at  $y^* = 10$ ; [(c) and (d)] variations of the fractional contribution to the mean flux from the four quadrants of the small-scale component of (c) MF and (d) HF as functions of  $k_f$  at  $y^* = 10$ . The data are taken from the case Ma00Re18K (red dashed lines), Ma08Re17K (blue dashed lines), and Ma15Re20K (black dashed lines).

Then we pay attention to the footprints of the logarithmic-region fluxes on the near-wall region  $y_i^* = 10$  with  $y_p^* = 100$ . Figures 13(a) and 13(b) show the fractional contribution of each quadrant for MF and HF, respectively. It can be found that the absolute value of FC of each quadrant decreases as the enlargement of the Mach number for  $k_f < 2$ . It implies that the compressibility lessens the linkages between the near-wall velocity and temperature fields and the energy-containing motions populating the logarithmic region slightly. Whether it holds at larger Mach numbers deserves further investigation. Figure 14 compares the length scale of the footprints in each quadrant of these cases. It is intriguing to find that the occurrence frequencies at a given  $l_x^*$  for the footprints are nearly identical for different Mach numbers. This observation provides evidence for the proposition in previous studies [42,43], which claimed that the statistical characteristics of the large-scale motions in the near-wall region scale well in the inner unit. For the small-scale fluxes,  $u'_{d,s}v'_d$  and  $T'_{d,s}v'_d$ , their fractional contribution of each quadrant are shown in Figs. 13(c) and 13(d). As can be seen, the contribution from each quadrant is not changed noticeably.

For the logarithmic region, the MF and the HF are decomposed into active and inactive parts for the cases Ma15Re20K and Ma08Re17K, and their contributions are compared in Fig. 15 along with the corresponding mean fluxes. It can be seen that the enlargement of the Mach number does not change the viscous scaled magnitudes of the MF and the HF at a fixed  $Re_\tau^*$  ( $Re_\tau^* \approx 780$ ). Though

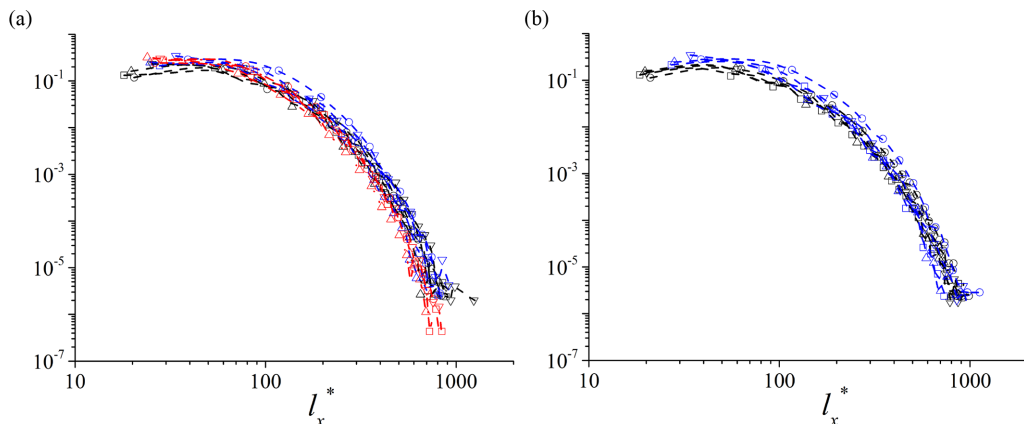


FIG. 14. Occurrence frequency of each  $l_x^*$  for the large-scale component of (a) MF and (b) HF at  $y^* = 10$ . The data are taken from the case Ma00Re18K (red dashed lines), Ma08Re17K (blue dashed lines), and Ma15Re20K (black dashed lines). Symbols as in Fig. 13.

their mean intensities are not altered significantly in the logarithmic region, the contribution from the inactive component decreases under the enhancement of the compressibility, especially for MF. The two components at  $y^* = 3.9\sqrt{\text{Re}_\tau^*}$  are studied separately for the corresponding four quadrants in Fig. 16 along with the results of the incompressible case Ma00Re18K. It can be observed that the alteration of the Mach number mainly affects the inactive weak events. To be specific, the absolute value of FC of each quadrant belonging to the inactive component decreases as the enlargement of the Mach number for  $k_f < 2$ . We also notice that the intensities of the events residing in each quadrant of the large-scale footprints in the near-wall region, namely the near-wall part of these inactive motions, also decrease with the enlargement of the Mach number [see Figs. 13(a) and 13(b)]. All these may suggest that the increase of the Mach number weakens the intensities of the momentum- and heat-flux events generated by the wall-attached motions as a whole. Whether this conjecture is valid at higher Mach numbers remains to be studied. Further investigations reveal that the impacts of the Mach number on HF in the logarithmic region are less than those of MF, which is consistent with the result shown in Fig. 15. For the outer region, no negligible difference in the statistical characteristics of MF and HF can be found for the cases with different Mach numbers at

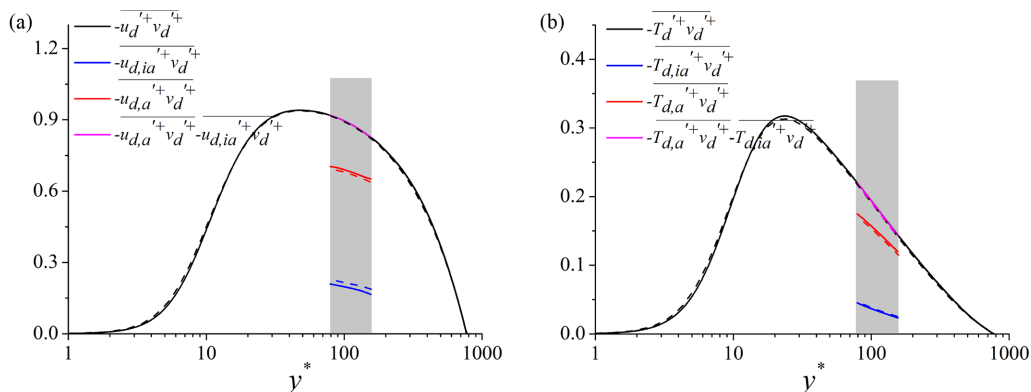


FIG. 15. Variations of the viscous scaled MF (a) and HF (b) as functions of  $y^*$  for the cases Ma15Re20K (solid lines) and Ma08Re17K (dashed lines). MF and HF are decomposed into active and inactive components in the logarithmic region indicated by the shaded regions in the figures.

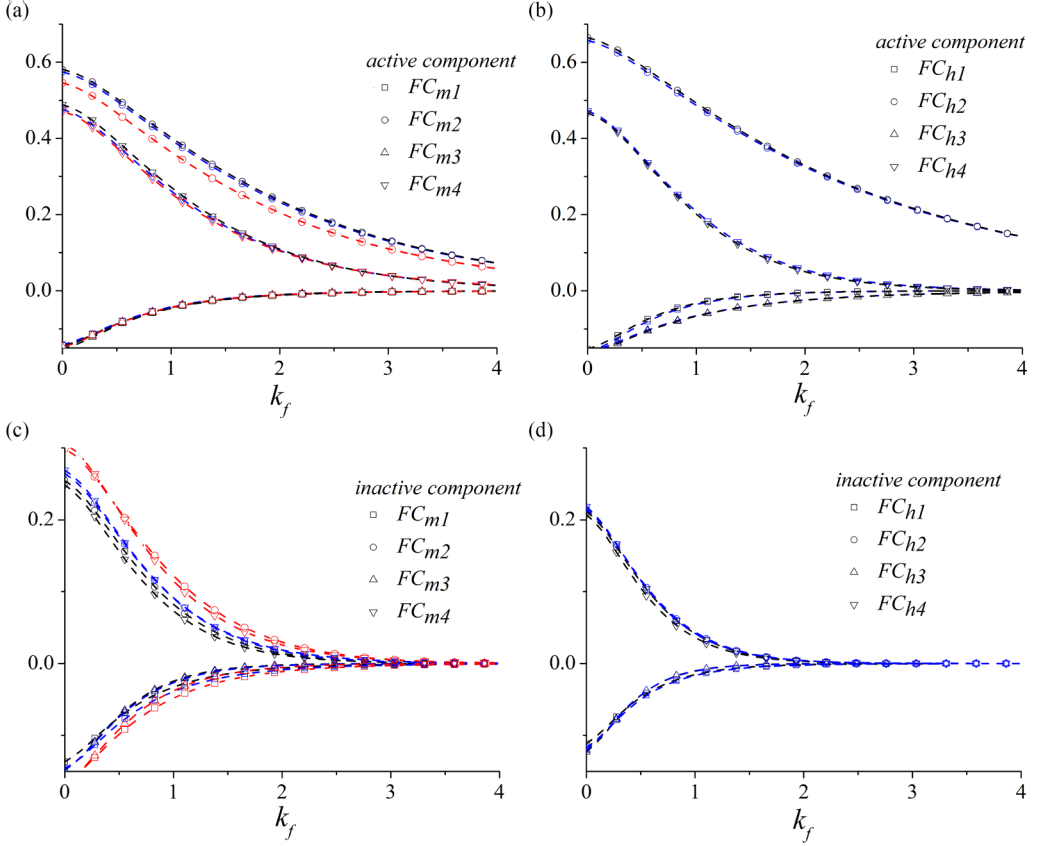


FIG. 16. [(a) and (b)] Variations of the fractional contribution to the mean flux from the four quadrants of the active (a) MF and (b) HF as functions of  $k_f$  at  $y^* = 3.9\sqrt{\text{Re}_\tau^*}$ ; [(c) and (d)] variations of the fractional contribution to the mean flux from the four quadrants of the inactive (c) MF and (d) HF as functions of  $k_f$  at  $y^* = 3.9\sqrt{\text{Re}_\tau^*}$ . The data are taken from the case Ma00Re18K (red dashed lines), Ma08Re17K (blue dashed lines), and Ma15Re20K (black dashed lines).

identical wall-normal positions (for instance,  $y/h = 0.5$ ), and thus we do not report them here in detail.

In summary, the Mach number effects can only be starkly observed in the footprints of the logarithmic-region fluxes on the near-wall region and the proportions of the inactive and the active components in the logarithmic region, whereas the MF and the HF in other wall-normal locations at desperate Mach numbers exhibit negligible differences. Intrinsically, the increase in compressibility diminishes the penetrability of the near-wall flow. It can be conjectured that the higher mean velocity and temperature gradients of the supersonic case near the wall may preclude the permeation of the wall-attached eddies. We will verify our proposition when the database at higher Mach numbers is formed.

## VI. CONCLUDING REMARKS

In the present study, we dissect the statistical characteristics of the momentum and heat fluxes in compressible turbulent channel flows via quadrant analysis by appealing to the newly built DNS database with different Mach and Reynolds numbers. To shed light on the scale interactions between

the inner and outer layers, we adopt the spectral linear stochastic estimation to decompose the signals at these locations. The conclusions are summarized below.

(a) In the near-wall region, the sweeps ( $Q_{m4}$  and  $Q_{h4}$ ) contribute most to their mean flux. Decomposing these two fluxes into large- and small-scale components suggests that the former is the footprints of large-scale eddies and rather uniform in physical space, whereas the latter is uneven in space and includes the strong transports of momentum and heat in the near-wall region.

(b) In the logarithmic region, the ejections ( $Q_{m2}$  and  $Q_{h2}$ ) contribute most to their mean flux. Both the inactive and active components of MF and HF are found to have contributions. The former accounts for 18%–20% of the mean flux, which is deemed to be negligible according to the classical attached-eddy model. We also show that these two components are not symmetric among the four quadrants.

(c) In the outer region, the ejections still contribute most to their mean flux. The ejections of HF are remarkably stronger than those of the MF, and the former is more sparse in the physical space.

(d) Reynolds number is shown to have a minor effect on the statistical characteristics of MF and HF. The enlargement of the Mach number only appears to lessen the linkages between the inner and outer region fluxes, adjust proportions of the inactive and active components in the logarithmic region and rarely alter the overall properties of HF and MF. Comparatively speaking, the HF in the compressible wall-bounded turbulence is more sensitive to the change of compressibility than the MF.

By employing the SLSE developed in previous studies to extract the velocity signals from the multiscale structures, the present work offers much insight into the MF and HF events in compressible turbulence. Overall speaking, they share substantial common features, at least within the cases under scrutinizing. This indicates that the Morkovin hypothesis is valid when the Mach number is not sufficiently high ( $M_b < 5$ ) [44] and that the thermodynamic fluctuations have insignificant effects on the turbulence structures. On the other hand, the findings of the present study demonstrate that the generation of the extreme events of the heat and momentum transfers in the near-wall region should be ascribed to the near-wall small-scale flow rather than the influences exerted by the large-scale motions populating the logarithmic and outer regions. This observation may be revealing for the development of drag-reduction and heat-control techniques. Finally, we also want to point out that the methodologies deployed in the present study can be extended to dissect the MF and the HF in supersonic or hypersonic boundary layers. For example, the alteration of the wall thermal condition is reported to modify the velocity and thermal streaks in the near-wall region of the compressible turbulent flat-plate boundary layers [31,45]. Hence, it is intriguing to shed light on this effect on the statistical characteristics of the MF and the HF by resorting to the current framework.

#### ACKNOWLEDGMENTS

L.F. acknowledges the fund from the Research Grants Council (RGC) of the Government of Hong Kong Special Administrative Region (HKSAR) with RGC/ECS Project (Grant No. 26200222), the fund from CORE as a joint research center for ocean research between QNLM and HKUST, and the fund from the Project of Hetao Shenzhen-Hong Kong Science and Technology Innovation Cooperation Zone (Grant No. HZQB-KCZYB-2020083).

- 
- [1] W. Willmarth and S. Lu, Structure of the Reynolds stress near the wall, *J. Fluid Mech.* **55**, 65 (1972).
  - [2] J. Wallace, H. Eckelmann, and R. Brodkey, The wall region in turbulent shear flow, *J. Fluid Mech.* **54**, 39 (1972).
  - [3] R. Narasimha, S. Kumar, A. Prabhu, and S. Kailas, Turbulent flux events in a nearly neutral atmospheric boundary layer, *Philos. Trans. R. Soc. A* **365**, 841 (2007).

- [4] R. Deshpande and I. Marusic, Characterising momentum flux events in high Reynolds number turbulent boundary layers, *Fluids* **6**, 168 (2021).
- [5] C. Cheng and L. Fu, Large-scale motions and self-similar structures in compressible turbulent channel flows, *Phys. Rev. Fluids* **7**, 114604 (2022).
- [6] S. Kline, W. Reynolds, F. Schraub, and P. Runstadler, The structure of turbulent boundary layers, *J. Fluid Mech.* **30**, 741 (1967).
- [7] S. Lu and W. Willmarth, Measurements of the structure of the Reynolds stress in a turbulent boundary layer, *J. Fluid Mech.* **60**, 481 (1973).
- [8] R. Blackwelder and R. Kaplan, On the wall structure of the turbulent boundary layer, *J. Fluid Mech.* **76**, 89 (1976).
- [9] J. Kim, Turbulence structures associated with the bursting event, *Phys. Fluids* **28**, 52 (1985).
- [10] D. Bogard and W. Tiederman, Burst detection with single-point velocity measurements, *J. Fluid Mech.* **162**, 389 (1986).
- [11] O. Flores and J. Jiménez, Hierarchy of minimal flow units in the logarithmic layer, *Phys. Fluids* **22**, 071704 (2010).
- [12] A. Lozano-Durán, O. Flores, and J. Jiménez, The three-dimensional structure of momentum transfer in turbulent channels, *J. Fluid Mech.* **694**, 100 (2012).
- [13] A. A. Townsend, *The Structure of Turbulent Shear Flow*, 2nd ed. (Cambridge University Press, Cambridge, UK, 1976).
- [14] A. Townsend, Equilibrium layers and wall turbulence, *J. Fluid Mech.* **11**, 97 (1961).
- [15] R. Deshpande, J. Monty, and I. Marusic, Active and inactive components of the streamwise velocity in wall-bounded turbulence, *J. Fluid Mech.* **914**, A5 (2021).
- [16] R. Mathis, N. Hutchins, and I. Marusic, Large-scale amplitude modulation of the small-scale structures in turbulent boundary layers, *J. Fluid Mech.* **628**, 311 (2009).
- [17] I. Marusic, R. Mathis, and N. Hutchins, Predictive model for wall-bounded turbulent flow, *Science* **329**, 193 (2010).
- [18] C. Cheng and L. Fu, Consistency between the attached eddy model and the inner outer interaction model: A study of streamwise wall shear stress fluctuations in a turbulent channel flow, *J. Fluid Mech.* **942**, R9 (2022).
- [19] S. Pirozzoli and M. Bernardini, Turbulence in supersonic boundary layers at moderate Reynolds number, *J. Fluid Mech.* **688**, 120 (2011).
- [20] X. Yuan, F. Tong, W. Li, J. Chen, and S. Dong, Wall-attached temperature structures in supersonic turbulent boundary layers, *Phys. Fluids* **34**, 115116 (2022).
- [21] X. Chen, C. Cheng, L. Fu, and J. Gan, Linear response analysis of supersonic turbulent channel flows with a large parameter space, *J. Fluid Mech.* **962**, A7 (2023).
- [22] D. Modesti and S. Pirozzoli, Reynolds and Mach number effects in compressible turbulent channel flow, *Int. J. Heat Fluid Flow* **59**, 33 (2016).
- [23] J. Yao and F. Hussain, Turbulence statistics and coherent structures in compressible channel flow, *Phys. Rev. Fluids* **5**, 084603 (2020).
- [24] L. Fu, M. Karp, S. Bose, P. Moin, and J. Urzay, Shock-induced heating and transition to turbulence in a hypersonic boundary layer, *J. Fluid Mech.* **909**, A8 (2021).
- [25] L. Fu, S. Bose, and P. Moin, Prediction of aerothermal characteristics of a generic hypersonic inlet flow, *Theor. Comput. Fluid Dyn.* **36**, 345 (2022).
- [26] C. Cheng and L. Fu, Linear-model-based study of the coupling between velocity and temperature fields in compressible turbulent channel flows, *J. Fluid Mech.* **964**, A15 (2023).
- [27] J. C. Del Álamo, J. Jiménez, P. Zandonade, and R. Moser, Scaling of the energy spectra of turbulent channels, *J. Fluid Mech.* **500**, 135 (2004).
- [28] G. Gerolymos and I. Vallet, Pressure, density, temperature and entropy fluctuations in compressible turbulent plane channel flow, *J. Fluid Mech.* **757**, 701 (2014).
- [29] K. Griffin, L. Fu, and P. Moin, Velocity transformation for compressible wall-bounded turbulent flows with and without heat transfer, *Proc. Natl. Acad. Sci. USA* **118**, e2111144118 (2021).

- [30] T. Bai, K. Griffin, and L. Fu, Compressible velocity transformations for various noncanonical wall-bounded turbulent flows, *AIAA J.* **60**, 4325 (2022).
- [31] J. Huang, L. Duan, and M. Choudhari, Direct numerical simulation of hypersonic turbulent boundary layers: Effect of spatial evolution and Reynolds number, *J. Fluid Mech.* **937**, A3 (2022).
- [32] W. Baars, N. Hutchins, and I. Marusic, Self-similarity of wall-attached turbulence in boundary layers, *J. Fluid Mech.* **823**, R2 (2017).
- [33] C. Cheng, W. Shyy, and L. Fu, Streamwise inclination angle of wall-attached eddies in turbulent channel flows, *J. Fluid Mech.* **946**, A49 (2022).
- [34] A. E. Perry and M. S. Chong, On the mechanism of wall turbulence, *J. Fluid Mech.* **119**, 173 (1982).
- [35] Y. Hwang, Statistical structure of self-sustaining attached eddies in turbulent channel flow, *J. Fluid Mech.* **767**, 254 (2015).
- [36] R. Adrian, Hairpin vortex organization in wall turbulence, *Phys. Fluids* **19**, 041301 (2007).
- [37] I. Marusic, W. J. Baars, and N. Hutchins, Scaling of the streamwise turbulence intensity in the context of inner-outer interactions in wall turbulence, *Phys. Rev. Fluids* **2**, 100502 (2017).
- [38] C. Cheng and L. Fu, A scale-based study of the Reynolds number scaling for the near-wall streamwise turbulence intensity in wall turbulence, *Int. J. Heat Fluid Flow* **101**, 109136 (2023).
- [39] L. Wang, R. Hu, and X. Zheng, A scaling improved inner–outer decomposition of near-wall turbulent motions, *Phys. Fluids* **33**, 045120 (2021).
- [40] R. Mathis, N. Hutchins, and I. Marusic, A predictive inner–outer model for streamwise turbulence statistics in wall-bounded flows, *J. Fluid Mech.* **681**, 537 (2011).
- [41] B. Ganapathisubramani, E. Longmire, and I. Marusic, Characteristics of vortex packets in turbulent boundary layers, *J. Fluid Mech.* **478**, 35 (2003).
- [42] Y. Hwang, Mesolayer of attached eddies in turbulent channel flow, *Phys. Rev. Fluids* **1**, 064401 (2016).
- [43] C. Cheng, W. Li, A. Lozano-Durán, and H. Liu, On the structure of streamwise wall-shear stress fluctuations in turbulent channel flows, *J. Fluid Mech.* **903**, A29 (2020).
- [44] M. V. Morkovin, Effects of compressibility on turbulent flows, *Mécanique de la Turbulence* (CNRS, Paris, 1962), pp. 367–380.
- [45] R. Hirai, R. Pecnik, and S. Kawai, Effects of the semi-local Reynolds number in scaling turbulent statistics for wall heated/cooled supersonic turbulent boundary layers, *Phys. Rev. Fluids* **6**, 124603 (2021).